Tangent double Hopf bifurcation in a differentially rotating cylinder flow

F. Marques*
Departament de Física Aplicada, Universitat Politècnica de Catalunya, Jordi Girona Salgado s/n, Mòdul B4 Campus Nord, 08034 Barcelona, Spain

A. Yu. Gelfgat†
Department of Fluid Dynamics and Heat Transfer, Faculty of Engineering, Tel-Aviv University, Ramat Aviv 69978, Tel-Aviv, Israel

J. M. Lopez‡
Department of Mathematics and Statistics, Arizona State University, Tempe, Arizona 85287, USA
(Received 4 December 2002; published 24 July 2003)

A tangent double Hopf bifurcation has been found in a rotating cylinder flow driven by the counter-rotation of the top endwall. The codimension-3 tangent double Hopf point has been located using linear stability analysis. The nonlinear analysis of the multiple solutions in a neighborhood of this bifurcation point is performed by numerical solutions of the three-dimensional Navier-Stokes equations. At the tangent double Hopf point, two rotating waves and an unstable modulated rotating wave bifurcate simultaneously. A center manifold/normal form analysis is also performed, which is in very good agreement with both the linear and nonlinear computations. By a detailed exploration of the nonlinear flow, we have unraveled the complex dynamics generated by the mode competition, which is organized by the codimension-3 tangent double Hopf bifurcation.

DOI: 10.1103/PhysRevE.68.016310 PACS number(s): 47.20.−k, 47.54.+r, 47.32.−y

I. INTRODUCTION

Systems in cylindrical geometries with internal shear layers have been widely studied from a number of perspectives. One of the motivations for these studies is that the instabilities of the shear layers in these laboratory flows mimic geophysical hydrodynamical behavior, such as planetary Rossby waves [1–4]. A feature that is ubiquitous in these systems is the competition between azimuthal modes with wave numbers m and $m+1$. A number of theoretical studies have qualitatively accounted for this mode competition in terms of the dynamics associated with double Hopf bifurcations [5–7].

A simple cylindrical system that produces an internal shear layer consists of flow in a cylinder, rotating with angular velocity Ω, that is driven by the differential rotation of the top lid with angular velocity Ω_t. The simplicity of this geometry allows for detailed laboratory experiments and numerical simulations. The basic axisymmetric state and its instability to three-dimensional modes, as well as a variety of secondary instabilities leading to multiple states, hysteresis, and chaotic dynamics have been studied in Refs. [8–10]. In particular, over extensive regions of parameter space, two rotating waves of azimuthal wave numbers $m=4$ and $m=5$ coexist and display a wealth of bifurcations/interactions that were explored in detail for a fixed height-to-radius ratio $\Lambda=H/R=0.5$ and a fixed angular velocity Ω.

Depending on the values of Λ and the ratio of angular frequencies $S=-\Omega/\Omega_t$, the first bifurcation as the Reynolds number $\mathrm{Re}=\Omega R^2/\nu$ (ν is the kinematic viscosity) is increased can be to a rotating wave with azimuthal wave number $m=4$ or $m=5$. Curves of double Hopf bifurcations, where both rotating waves bifurcates simultaneously, can also be obtained. The feature we have found is that for a specific point in the three-parameter space (Λ,S,Re), a collision of two double Hopf points takes place, producing a degenerate double Hopf bifurcation that has not been reported previously in the literature. The analysis of this new codimension-3 bifurcation, which organizes the mode competition in the particular fluid problem under consideration, is the object of the present study.

The paper is organized as follows. The flow geometry, symmetry, governing parameters, and equations are presented in Sec. II. In Sec. III, the normal form of the new bifurcation is analyzed, stressing the similarities and differences with the nondegenerate codimension-2 double Hopf bifurcation. The numerical methods used for the linear stability analysis and nonlinear three-dimensional Navier-Stokes solver, used to locate the degenerate double Hopf bifurcation and explore the associated nonlinear dynamics, are presented in Secs. IV A and IV B. The technical details of the normal form analysis are presented in Sec. IV C. The numerical results are presented and compared with the predictions from the center manifold/normal form theory in Sec. IV. Further, the structure of the rotating waves and how the tangent double Hopf bifurcation organizes their competition is provided in that section. Conclusions and discussion are presented in Sec. V.

II. FLOW GEOMETRY, SYMMETRY, GOVERNING PARAMETERS, AND EQUATIONS

The flow geometry is shown schematically in Fig. 1. It consists of a cylinder of radius R and height H, closed at the

*Electronic address: marques@fa.upc.es
†Electronic address: gelfgat@eng.tau.ac.il
‡Electronic address: lopez@math.asu.edu

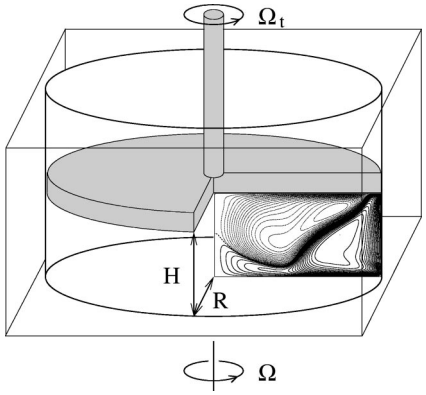

FIG. 1. Schematic representation of the flow geometry. The inset illustrates typical streamlines of a steady axisymmetric flow determined by numerical simulation.

bottom, rotating at rate $\Omega>0$, and containing an incompressible fluid of kinematic viscosity ν. The flow is driven by a contact top lid that rotates in the inertial frame of reference at rate Ω_t. We use R as the length scale and $1/\Omega$ as the time scale. There are three nondimensional parameters governing this system,

$$\mathrm{Re}=\Omega R^2/\nu,$$

$$\Lambda=H/R,$$

$$S=-\Omega_t/\Omega.$$

The domain in nondimensional cylindrical coordinates (r,θ,z) is

$$\mathcal{D}=\{0\leqslant r<1,0\leqslant\theta<2\pi,0<z<\Lambda\}.$$

Here, we consider the retrograde driving situation with $\Omega_t<0$, so that S is positive. In this situation, for small S there is radial inflow in the boundary layer on the differentially rotating upper lid. For sufficiently large S, this layer separates before reaching the axis and an internal shear layer forms. The shear layer separates fluid with azimuthal velocity of the same sense as the base of the cylinder from that with the sense of the counter-rotating top. There is also a strong meridional jetlike flow along the shear layer.

The governing equations, Navier-Stokes and conservation of mass, together with the boundary conditions, no-slip on all solid walls and regularity on the cylinder axis, are invariant with respect to rotations about the axis. The system possesses the symmetry group SO(2). The basic state for this system is a steady axisymmetric swirling flow with nontrivial structure in r and z, the radial and axial coordinates. A detailed study of the axisymmetric basic state and its stability in an axisymmetric subspace were presented in Refs. [9,10]. A typical axisymmetric basic state is shown in the inset of Fig. 1. The shear layer in this example separates near the upper right corner and reattaches at about mid-depth on the axis.

The equations governing the flow are the Navier-Stokes equations together with initial and boundary conditions. We denote the velocity vector and pressure, respectively, by $\mathbf{u}=(u,v,w)^T$ and p. The Navier-Stokes equations in velocity-pressure formulation written in cylindrical coordinates are

$$\partial_t u+a_r=-\partial_r p+\frac{1}{\mathrm{Re}}\left(\Delta u-\frac{1}{r^2}u-\frac{2}{r^2}\partial_\theta v\right),$$

$$\partial_t v+a_\theta=-\partial_\theta p+\frac{1}{\mathrm{Re}}\left(\Delta v-\frac{1}{r^2}v+\frac{2}{r^2}\partial_\theta u\right), \qquad (1)$$

$$\partial_t w+a_z=-\partial_z p+\frac{1}{\mathrm{Re}}\Delta w,$$

$$\frac{1}{r}\partial_r(ru)+\frac{1}{r}\partial_\theta v+\partial_z w=0, \qquad (2)$$

where

$$\Delta=\partial_r^2+\frac{1}{r}\partial_r+\frac{1}{r^2}\partial_\theta^2+\partial_z^2$$

is the Laplace operator in cylindrical coordinates and

$$a_r=u\partial_r u+\frac{v}{r}\partial_\theta u+w\partial_z u-\frac{v^2}{r},$$

$$a_\theta=u\partial_r v+\frac{v}{r}\partial_\theta v+w\partial_z v-\frac{uv}{r},$$

$$a_z=u\partial_r w+\frac{v}{r}\partial_\theta w+w\partial_z w. \qquad (3)$$

The equations are completed with admissible initial and boundary conditions. Computations are started either from an initial state of rest, or a solution at one point in parameter space is used as the initial condition for a nearby point in parameter space. The boundary conditions are no-slip on all solid walls and the essential pole conditions on the rotation axis (see Ref. [11] for details).

At low Reynolds number, the basic state is steady and axisymmetric, and can be easily computed using a variety of different methods [9–13]. The linear stability of this basic state can be analyzed by linearizing the Navier-Stokes equations. Substitution of $\{u,v,w,p\}=\{u_B,v_B,w_B,p_B\}+\{u_p,v_p,w_p,p_p\}$ in Eq. (1), where subscripts B denote the basic state and p the perturbations, and linearization gives the same equations (1) for the perturbations, except that the nonlinear terms are now

$$a_r=u_B\partial_r u+u\partial_r u_B+\frac{v_B}{r}\partial_\theta u+w_B\partial_z u+w\partial_z u_B-\frac{2vv_B}{r},$$

$$a_\theta=u_B\partial_r v+u\partial_r v_B+\frac{v_B}{r}\partial_\theta v+w_B\partial_z v+w\partial_z v_B-\frac{u_B v+uv_B}{r},$$

$$a_z=u_B\partial_r w+u\partial_r w_B+\frac{v_B}{r}\partial_\theta w+\partial_z(w_B w). \qquad (4)$$

The numerical methods used to determine the linear stability of the basic state to general three-dimensional perturbations and to study the nonlinear dynamics are briefly described in Secs. IV A and IV B.

III. BACKGROUND ON DOUBLE HOPF BIFURCATIONS

For some low-codimension bifurcations, dynamical systems theory provides a center manifold reduction of the high dimensional system (e.g., Ref. [14]) and a *normal form*, a low-dimensional, low-order polynomial system that captures the dynamics of the full nonlinear system in the neighborhood of the bifurcation (e.g., Ref. [15]). The normal form contains a number of parameters that unfold the bifurcation; the number of parameters being the codimension of the bifurcation considered. Arbitrary perturbations of the normal form are usually accounted for by these unfolding parameters (see Ref. [16] for details and examples). In this case, arbitrary perturbations result in a topologically equivalent system preserving all the dynamics of the normal form; this is the case for the well-known local codimension-1 bifurcations [17]. However, when the codimension of the system is 2 or greater, persistence of the normal form is not always guaranteed. One may still perform a normal form analysis on the original system, truncate at some finite (low) order and extract some of the characteristic dynamics of the original system. However, this formal application of the theory results in a *formal normal form* with, in general, some dynamical features that do not persist upon perturbation. The double Hopf bifurcation is a typical example where the dynamics of the formal normal form do not always persist.

The infinite-dimensional phase space of our problem, in certain regions of parameter space, admits a four-dimensional center manifold parametrized by a pair of amplitudes $r_{1,2}$ and angles $\phi_{1,2}$. The normal form is given by [17]

$$\dot{r}_1 = r_1[f_1(\alpha_{1,2}) + p_{11}r_1^2 + p_{12}r_2^2 + s_1 r_2^4],$$

$$\dot{r}_2 = r_2[f_2(\alpha_{1,2}) + p_{21}r_1^2 + p_{22}r_2^2 + s_2 r_1^4],$$

$$\dot{\phi}_1 = \omega_1,$$

$$\dot{\phi}_2 = \omega_2,$$

where the two pairs of complex conjugate eigenvalues are $\pm i\omega_{1,2}$ at the bifurcation point $\alpha_{1,2}=0$; $f_{1,2}$ are functions of the parameters of the system, $\alpha_{1,2}$. The $\omega_{1,2}$, p_{ij}, and s_i depend on the parameters $\alpha_{1,2}$ and satisfy certain nonresonant and nondegeneracy conditions in the neighborhood of the bifurcation:

$$m_1\omega_1 \neq m_2\omega_2, \tag{5}$$

$$p_{ij} \neq 0, \tag{6}$$

where m_1, m_2 are the azimuthal wave numbers of the two bifurcated rotating waves [18]. If the functions $f_{1,2}$ satisfy the additional nondegeneracy condition

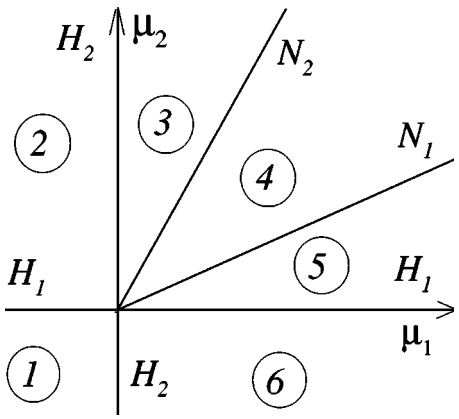

FIG. 2. Bifurcation diagram for a simple type I double Hopf bifurcation. The curves H_1 and H_2 (coinciding with the axes μ_1 and μ_2, respectively) are the two Hopf bifurcation curves at which the limit cycles, P_1 and P_2, bifurcate supercritically from the basic state P_0. The curves N_1 and N_2 are Neimark-Sacker bifurcation curves at which the quasiperiodic mixed-mode P_3 bifurcates. Phase portraits in each of the six regions indicated are shown in Fig. 3.

$$\det\left(\frac{\partial f_{1,2}}{\partial \alpha_{1,2}}\right)\Bigg|_{\alpha=0} \neq 0, \tag{7}$$

the two Hopf bifurcation curves given by $f_{1,2}=0$ intersect transversally, and introducing the new independent parameters $\mu_{1,2}=f_{1,2}$, we arrive at the normal form for the nondegenerate double Hopf bifurcation analyzed in detail in Ref. [17]:

$$\dot{r}_1 = r_1(\mu_1 + p_{11}r_1^2 + p_{12}r_2^2 + s_1 r_2^4),$$

$$\dot{r}_2 = r_2(\mu_2 + p_{21}r_1^2 + p_{22}r_2^2 + s_2 r_1^4),$$

$$\dot{\phi}_1 = \omega_1,$$

$$\dot{\phi}_2 = \omega_2. \tag{8}$$

The normal form (8), in the nondegenerate case, admits a multitude of distinct dynamical behavior, depending on the values of p_{ij} and s_i. These are divided into so-called *simple* ($p_{11}p_{22}>0$) and *difficult* ($p_{11}p_{22}<0$) cases. In the simple cases, the topology of the bifurcation diagram is independent of the s_i terms. Even in the simple case, several different bifurcation diagrams exist. A comprehensive description of all the simple and difficult scenarios is given in Ref. [17]. In our problem, away from the tangent double Hopf point in parameter space, the nondegenerate double Hopf bifurcations are of simple type (type I, simple, in the classification of Ref. [17]). This behavior is typically encountered when the Hopf bifurcations are supercritical from the stable basic state [18–20]. Figure 2 shows the bifurcation diagram in a neighborhood of a nondegenerate double Hopf bifurcation point in parameter space, corresponding to our problem. The parameter space is divided into six regions, delimited by bifurcation curves. The number of solutions and their stability are different in each region. Figure 3 shows typical phase por-

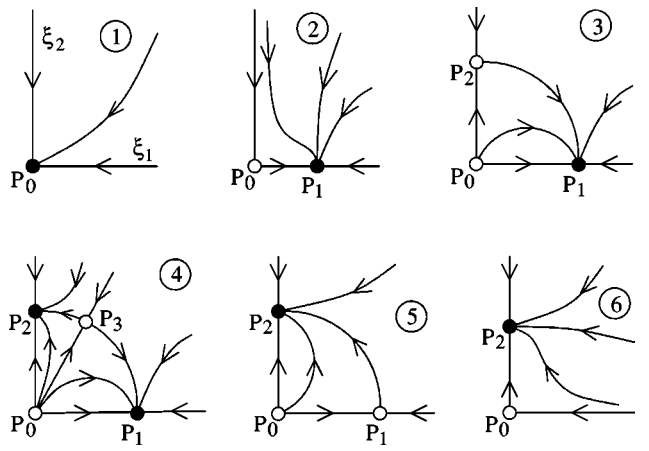

FIG. 3. Phase portraits corresponding to the different regions of the double Hopf and tangent double Hopf bifurcations considered here. Solid (open) circles are stable (unstable) states.

traits in these six different regions. P_1 and P_2 are rotating waves emerging from the basic state when the Hopf curves H_1 and H_2 are crossed. There is a region (4 in Fig. 2) where both rotating waves coexist and are stable. In this region an unstable two-torus solution (a modulated rotating wave) exists, and its presence allows P_1 and P_2 to be simultaneously stable.

We have located a point in parameter space where the two Hopf bifurcation curves are tangent. In this case, the nondegeneracy condition (7) is not satisfied, and the double Hopf bifurcation is degenerate. The linear parts of f_1 and f_2 are proportional to each other, and they differ at second order. By an appropriate redefinition of the parameters, we can write

$$f_1 = a\mu_2, \quad f_2 = \mu_2 - \mu_1^2; \tag{9}$$

where a is the proportionality constant between the linear parts of $f_{1,2}$. In the parameter space $\mu_{1,2}$, the two Hopf bifurcation curves are the straight line $\mu_2 = 0$ and the parabola $\mu_2 = \mu_1^2$. But the tangency is not a generic condition, and introduction of additional parameters (or perturbations) will break the tangency. In order to unfold this degeneracy, a third parameter must be introduced; the tangent double Hopf (TdH) bifurcation is a codimension-3 bifurcation. The three parameters are related to the three physical governing parameters Re, Λ, and S. The final form of the functions $f_{1,2}$ is

$$f_1 = a\mu_2, \quad f_2 = \mu_2 - \mu_1^2 - \mu_3. \tag{10}$$

The normal form (8), in the nondegenerate case, admits a multitude of distinct dynamical behavior, depending on the values of p_{ij} and s_i. In the TdH degenerate case, the situation is more complex. Of all the possible cases, we analyze here the one that corresponds to our particular problem. As mentioned before, the bifurcation is of simple type, and the normal form, after appropriate changes of variables (which are exactly the same as in the nondegenerate double Hopf bifurcation, and are described in detail in Ref. [17]) can be written as

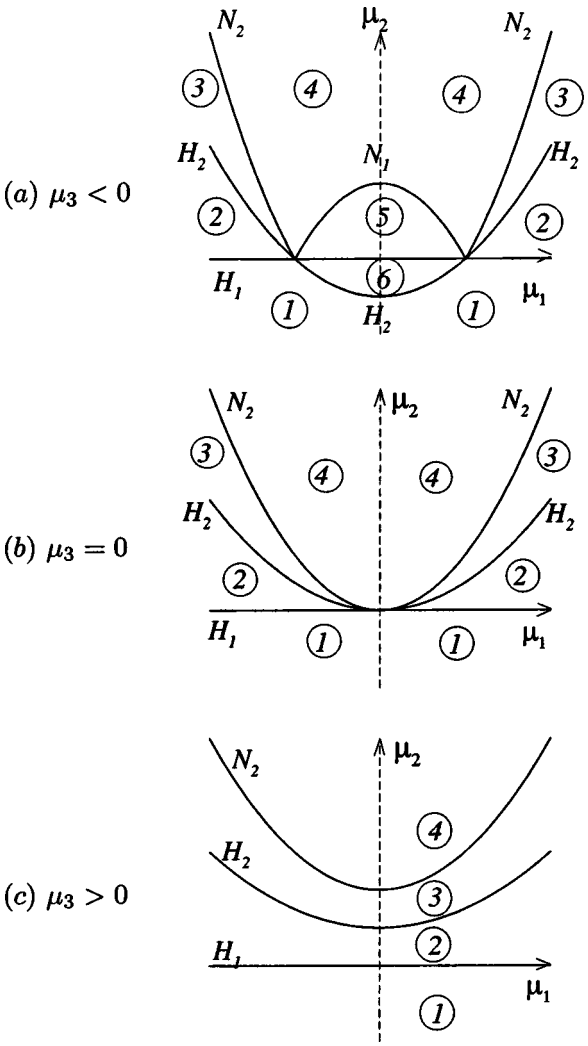

FIG. 4. Bifurcation diagrams for μ_3 as indicated.

$$\dot{\xi}_1 = \xi_1(a\mu_2 - \xi_1 - \eta\xi_2),$$

$$\dot{\xi}_2 = \xi_2(\mu_2 - \mu_1^2 - \mu_3 - \delta\xi_1 - \xi_2), \tag{11}$$

where a, η, and δ are nonzero constants, satisfying the conditions $\eta > a > 1/\delta > 0$; see Eq. (C1). The detailed analysis of the fixed point solutions of this system is given in Sec. IV C. Here we present a summary of the most important features.

Figure 4 shows the bifurcation diagram in a neighborhood of the tangent double Hopf bifurcation. Figure 4(a) corresponds to $\mu_3 < 0$, where the two Hopf curves H_1 and H_2 intersect transversally at two different points, two nondegenerate double Hopf points that exhibit the six regions displayed in Fig. 2. The new feature here is that the two Neimark-Sacker curves N_1 merge into a single curve that starts and ends at the two double Hopf points. Figure 4(b) corresponds to $\mu_3 = 0$, where the two Hopf curves H_1 and H_2 become tangent at the codimension-3 tangent double Hopf point. When the two double Hopf points in Fig. 4(a) merge, regions 5 and 6, the Neimark-Sacker curve N_1 disappears. We are left with three bifurcation curves, H_1, H_2, and N_2, simultaneously tangent at the degenerate tangent double

Hopf point. For $\mu_3>0$, these three bifurcation curves separate, as shown in Fig. 4(c). The important feature here is that when we have an ordinary Hopf curve H_1 with a secondary Hopf curve H_2 closeby, we will always find a subsequent Neimark-Sacker curve N_2, even though there is no intersection between H_1 and H_2. Beyond curve N_2, the two limit cycles (rotating waves in our case) coexist and are simultaneously stable. This is precisely the situation observed experimentally and numerically in Ref. [8], in the parameter space region $\Lambda=0.5$, Re$=1000$, and $S\in[0.4,0.8]$.

IV. RESULTS

A. Linear stability

The results of an extensive parametric study in (Λ, S, Re) space are summarized in Fig. 5. The stability to perturbations with azimuthal wave numbers $m\in[0,13]$ has been examined over an extensive range in parameter space, and the two modes $m=4$ and $m=5$ have been found to be the most dangerous. The figure shows the projection of the Hopf bifurcation manifolds [two-dimensional surfaces in (Λ, S, Re) space] for the onset of RW_4 and RW_5 onto (S, Re) space for three values of $\Lambda=0.55$, 0.56, and 0.57. These serve to indicate that at the point ($\Lambda\approx0.56$, Re≈349.5, $S\approx1.0$), the two Hopf bifurcation manifolds become tangent. The behavior in the neighborhood of this codimension-3 (TdH) point is consistent with generic TdH normal form theory involving supercritical Hopf bifurcations (see details in Sec. IV C and compare Figs. 5 and 15). In the following section, we explore the nonlinear dynamics in the neighborhood of the TdH using the fully nonlinear three-dimensional Navier-Stokes solver, which amongst other details, shows that the associated Hopf bifurcations to RW_4 and RW_5 are supercritical.

B. Nonlinear computations

The Hopf bifurcation curves have also been computed using the three-dimensional Navier-Stokes solver. We begin with computations in the axisymmetric subspace in order to obtain the steady axisymmetric base state. This base state with an added nonaxisymmetric perturbation is used as the initial condition in the three-dimensional computations. The eigenvalues corresponding to the different azimuthal modes are determined from the observed linear growth/decay of the perturbations. Figure 6 shows the real part λ of the eigenvalues for azimuthal modes $m=4$ and 5. As the linear growth is very small near the bifurcation point, we have obtained the bifurcation curve (corresponding to $\lambda=0$) by linear interpolation. Nevertheless, the dependence of λ on Re is given very accurately by straight lines (as can be seen from Fig. 6), and the error due to the linear interpolation is negligible.

The critical Re for the Hopf bifurcations to RW_4 and RW_5 over a range of S and Λ in the neighborhood of the tangent double Hopf have now been determined by two independent numerical approaches, linear stability analysis and nonlinear computations. These results are summarized in Table I; the difference in the estimate of the critical Re is about 0.3%. This good agreement provides confidence in both methods.

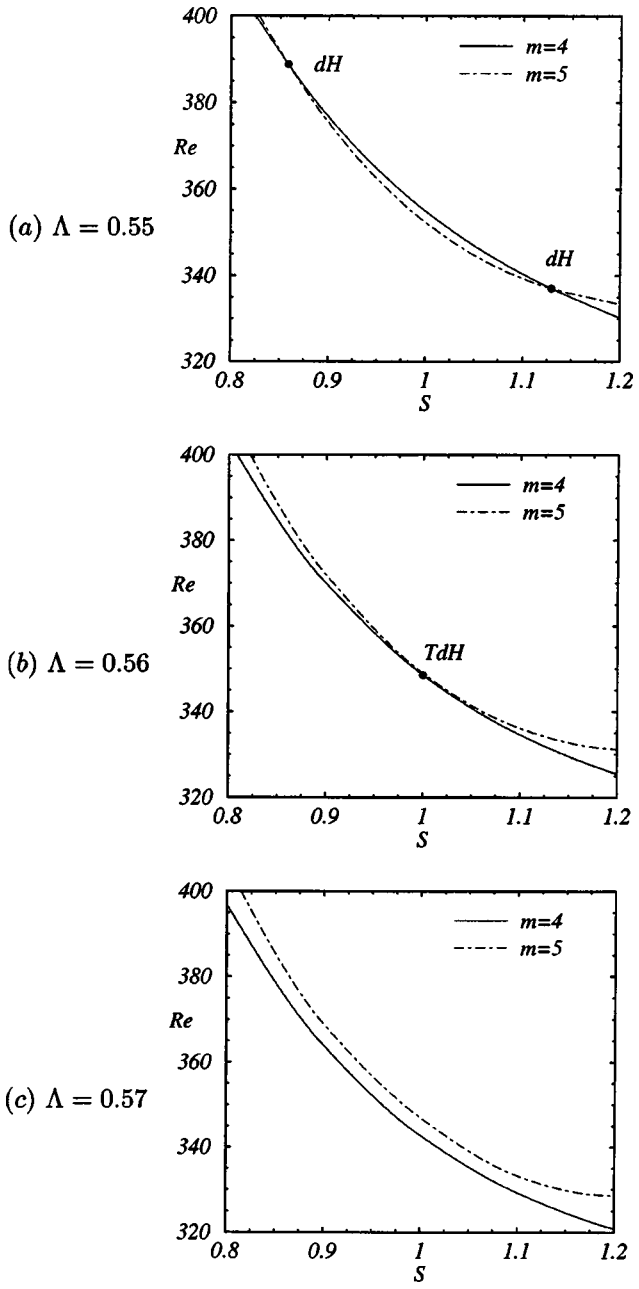

FIG. 5. Hopf bifurcation curves, determined by linear stability analysis, for the onset of RW_4 (solid line) and RW_5 (dashed line) in (S, Re) space for Λ as indicated. Double Hopf points (dH) and the tangent double Hopf point (TdH) are labeled.

In these Hopf bifurcations, rotating waves with azimuthal wave numbers $m=4$ and $m=5$, RW_4 and RW_5, emerge. These new solutions may be stable or unstable. Restricting the nonlinear computations to convenient invariant subspaces, they can be computed with the time evolution code. For example, computing RW_4 in the subspace C_4 containing only Fourier modes that are multiples of 4, we can compute a RW_4 that is unstable to perturbations with azimuthal wave numbers different from 0,4,8, . . . , because these perturbations do not belong to C_4. The dominant nonaxisymmetric modes are $m=4$ and 5, which are relatively primes, therefore mode 5 is not present in C_4, and mode 4 is not present in C_5,

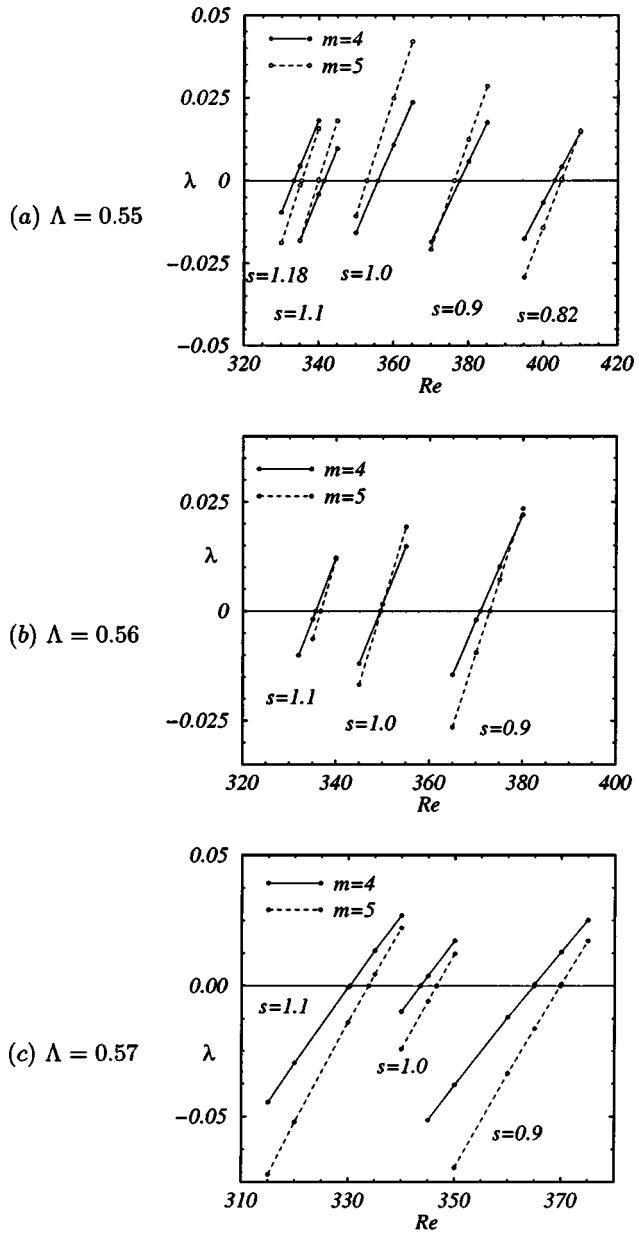

FIG. 6. Hopf bifurcations from the basic state, determined from nonlinear computations; λ is the real part of complex conjugate Hopf eigenvalues. The curves $\lambda=0$ for $m=4$ and $m=5$ correspond to the curves H_1 and H_2, respectively, in Fig. 4, and also to the solid and dashed curves in Fig. 5

so both states can be computed by time evolution in the corresponding subspace, regardless of their stability.

The Neimark-Sacker bifurcations of the rotating waves RW_4 and RW_5 can be computed in the same way that the Hopf bifurcations were computed. We use the computed RW_4 and RW_5 as initial conditions, adding a generic nonaxisymmetric perturbation. The observed linear growth/decay of the perturbations allows the computation of the most dangerous Floquet exponent (the equivalent of an eigenvalue for a limit cycle solution, see, e.g., Ref. [21]). Figure 7 shows the real part of the most dangerous Floquet exponent, γ (note that for Neimark-Sacker bifurcations, the Floquet exponents are complex conjugate pairs), for each of the rotating waves

TABLE I. Comparison between the linear and nonlinear codes. The critical Re numbers for the transitions between the base state and the rotating waves RW_4 and RW_5 are shown for Λ and S as indicated.

		$m=4$		$m=5$	
Λ	S	Linear	Nonlinear	Linear	Nonlinear
0.55	0.9	377.67	376.69	376.29	375.34
	1.0	355.88	354.94	352.94	352.34
	1.1	341.50	340.41	339.97	339.36
0.56	0.9	370.89	369.96	372.90	371.95
	1.0	349.46	348.56	349.62	348.97
	1.1	335.66	334.61	336.73	336.13
0.57	0.9	364.92	363.89	369.86	368.92
	1.0	343.60	342.76	346.62	346.97
	1.1	330.39	329.29	333.90	333.26

RW_4 and RW_5. The bifurcation curve (for $\gamma=0$) has been obtained by quadratic interpolation to all the computed data, because in this case the dependence of the growth rate γ on Re is not linear (for Hopf bifurcations, λ, the growth rate, is linear with Re near the bifurcation).

Figure 8 shows the Hopf and Neimark-Sacker bifurcation curves obtained, along with the different solutions computed. Solid curves correspond to the Hopf bifurcation from the basic state to RW_4, dashed curves to the Hopf bifurcation from the basic state to RW_5, and dotted curves are the Neimark-Sacker bifurcation curves. Different symbols represent the different types of solutions obtained. The agreement with the normal form theory developed in Sec. III is complete (compare Figs. 4 and 8).

C. Structure of the bifurcated solutions

The case $S=0$ corresponds to solid-body rotation. As S is increased, the counter-rotation of the top lid produces a countermeridional flow near the axis and the top lid. This counterflow results in the separation of the top-lid boundary layer and the development of a shear layer into the interior that separates the two counter-rotating meridional flows. These two regions also have azimuthal flows with opposite senses; the shear in the layer is primarily in the azimuthal direction. The shear layer also has a jetlike profile in the meridional direction. It is the instability of this shear layer, via supercritical Hopf bifurcations, to azimuthal modes with wave numbers 4 and 5 that leads to the bifurcated rotating waves RW_4 and RW_5 (see Ref. [8] for details).

As $S\rightarrow 1$, the top-lid boundary layer separation point approaches the corner $(r=1,\ z=\Lambda)$. It is in this parameter regime that the mode competition between RW_4 and RW_5 leads to the tangent double Hopf dynamics. Figure 9 shows contours of streamlines and azimuthal velocity as well as velocity vectors projected onto a meridional plane for two basic states with $(\mathrm{Re}=370,\ S=0.9)$ and $(\mathrm{Re}=335,\ S=1.1)$, both at $\Lambda=0.56$. At these two points, the basic state is on the verge of becoming unstable, and they straddle the tangent double Hopf point.

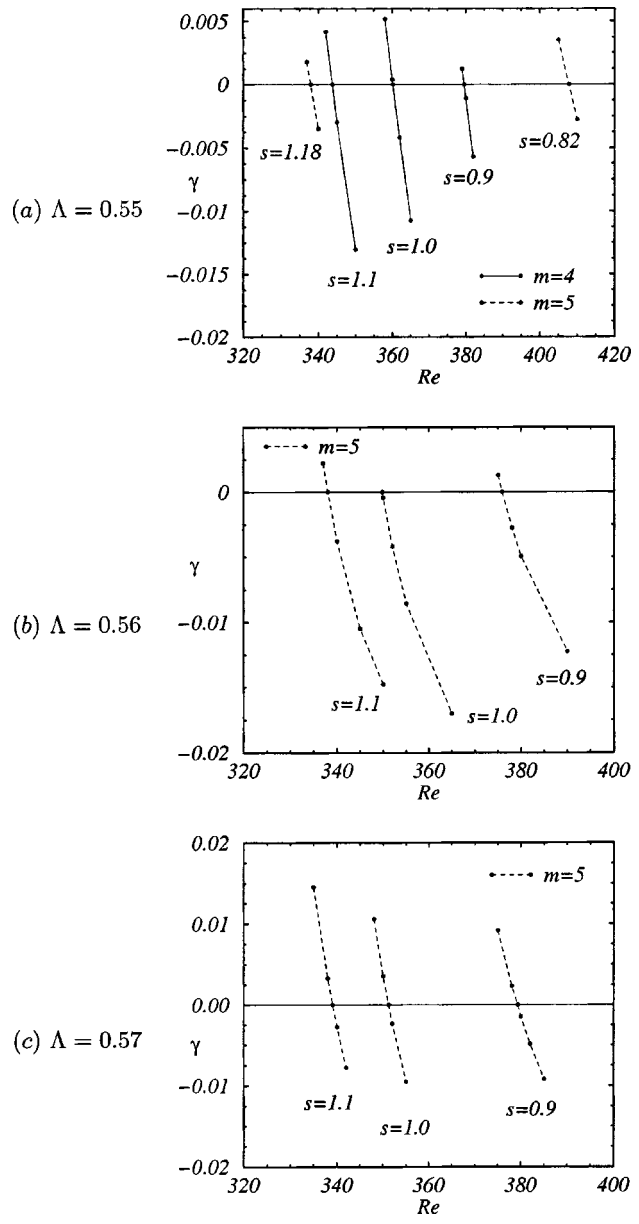

FIG. 7. Neimark-Sacker bifurcations from the limit cycles RW_4 and RW_5; γ is the real part of the complex conjugate Floquet exponents. The curves $\gamma=0$ for $m=4$ and $m=5$ correspond to the curves N_1 and N_2, respectively, in Fig. 4.

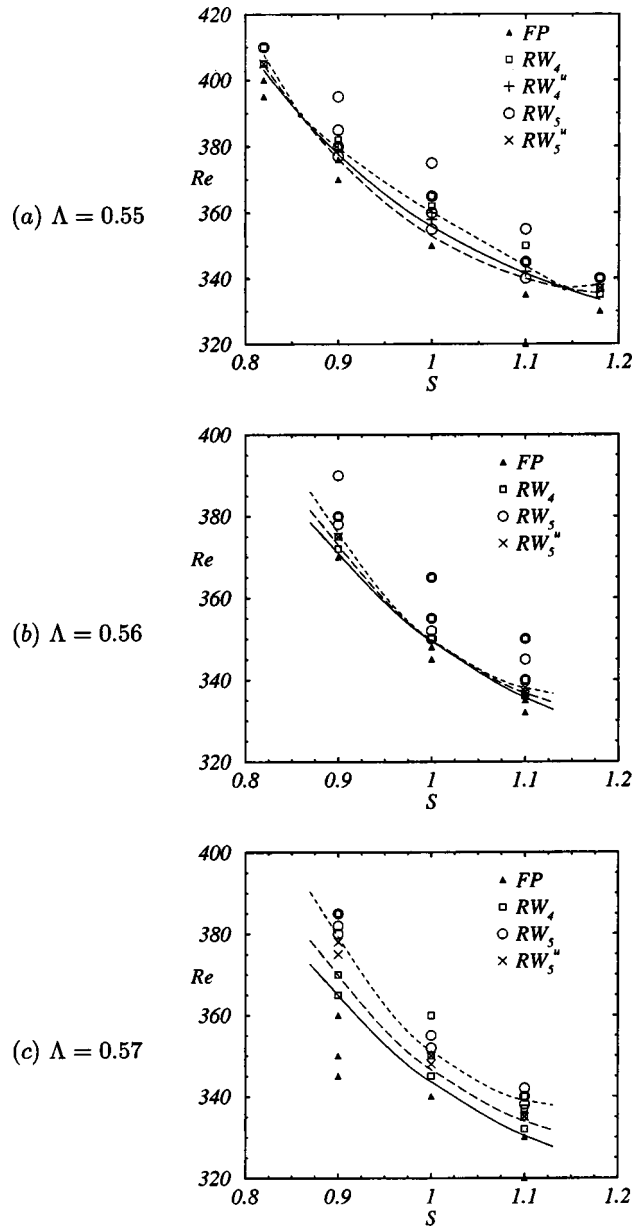

FIG. 8. Computed bifurcation diagrams for $\Lambda=0.55$, 0.56, 0.57. Computed solutions: basic state, ▲; RW_4 stable, □; RW_4 unstable +; RW_5 stable ○; RW_5 unstable, ×. Fitted bifurcation curves: basic state $\rightarrow RW_4$, solid; basic state $\rightarrow RW_5$, dashed; Neimark-Sacker curves, dotted.

The precession frequencies of RW_4 and RW_5 are shown in Fig. 10 for $\Lambda=0.55$, 0.56, 0.57, $S=0.9$, 1.0, 1.1, and $\mathrm{Re}\in(320,420)$. Over this entire range, the precession frequency is about 1/3 of the rotating frequency of the cylinder, and the waves rotate prograde with the cylinder. For given S there is little variation in the frequencies with Re or Λ, but it decreases substantially with increasing S. As the top counter-rotates faster with increasing S, the precession of the waves slows down.

For a double Hopf bifurcation with SO(2) symmetry to be resonant, the ratio of wave numbers must equal the ratio of precession frequencies (see Ref. [18]). From Fig. 10, we have that at the tangent double Hopf bifurcation point, the precession frequency ratio is $\omega_4/\omega_5\approx 0.93$—clearly not 4/5, and so our tangent double Hopf bifurcation satisfies Eq. (5) and is not resonant.

We now examine the bifurcated rotating wave states at a point in parameter space near the tangent double Hopf bifurcation where both RW_4 and RW_5 coexist and are stable. This point is ($\mathrm{Re}=365$, $S=1.0$, $\Lambda=0.55$) and is located in region 4 as indicated in Fig. 4(a); the corresponding schematic phase portrait is number 4 in Fig. 3. The rotating waves are three-dimensional spatial structures that are invariant in time and the whole structure precesses at a constant rate. They have C_m symmetry, i.e., they are invariant to discrete azimuthal rotations of $2\pi/m$. Further, rotations in space are equivalent to time evolution. The kinetic energy density of

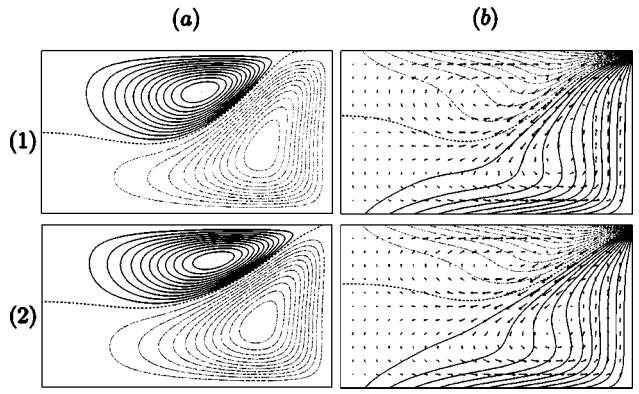

FIG. 9. Basic states at (1) (Re=370, $S=0.9$, $\Lambda=0.56$) and (2) (Re=335, $S=1.1$, $\Lambda=0.56$); showing (a) streamlines and (b) contours of the azimuthal velocity v and arrows of the (u,w) velocity components. These contours are shown in a meridional plane $(r,z)\in[0,1]\times[0,\Lambda]$, whose orientation is as in Fig. 1.

the mth azimuthal mode $\mathcal{E}_m(r,z)$ is used to identify the physical mechanism leading to the instability of the basic state, where

$$\mathcal{E}_m(r,z)=\frac{1}{2}\int_0^{2\pi}\mathbf{u}_m\cdot\mathbf{u}_m^* r\,d\theta.$$

Figure 11 shows contours of $\mathcal{E}_m(r,z)$ for (a) $m=4$ and (b) $m=5$, corresponding to RW_4 and RW_5, respectively, together with the velocity of the basic state projected onto a

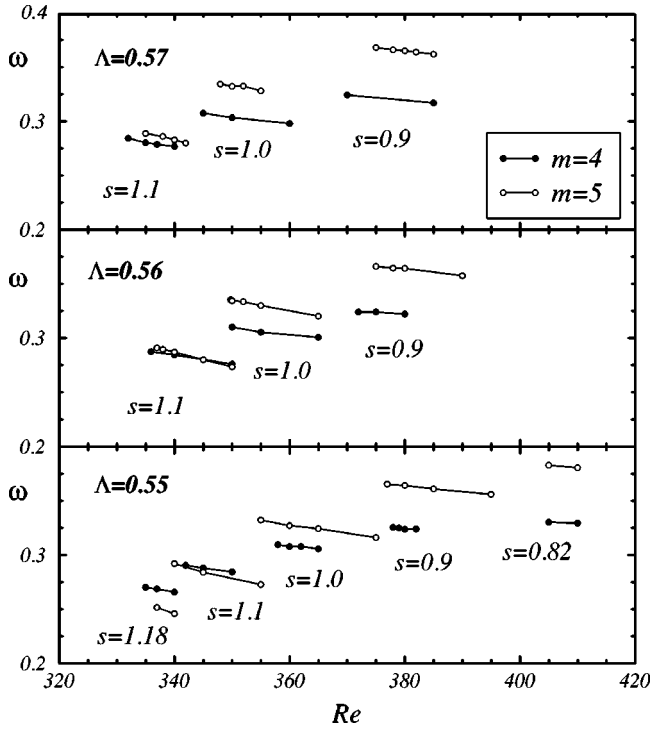

FIG. 10. Precession frequencies of the RW_4 and RW_5 rotating waves, for the solutions shown in Fig. 8. Solid and open circles correspond to RW_4 and RW_5 states, respectively.

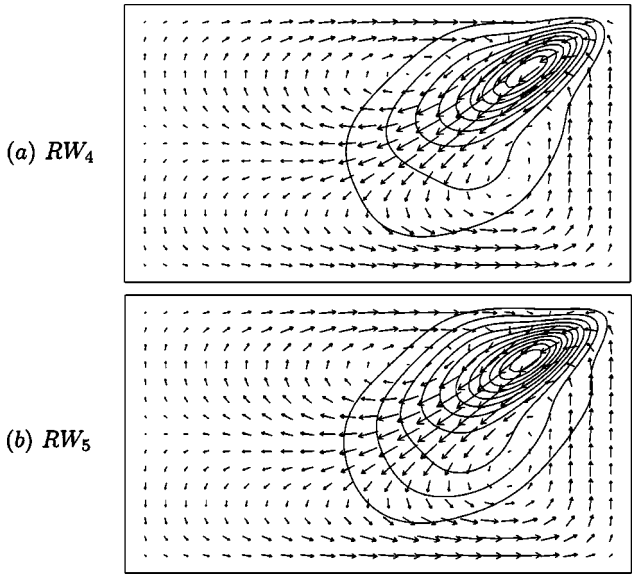

FIG. 11. Contours of $\mathcal{E}_m(r,z)$ and projections of the basic state velocity vectors onto a meridional plane, $(r,z)\in[0,1]\times[0,\Lambda]$, for (a) RW_4 ($m=4$) and (b) RW_5 ($m=5$) at (Re=365, $S=1.0$, $\Lambda=0.55$).

meridional plane. $\mathcal{E}_m(r,z)$ is localized about the separated shear layer and has a maximum near the point of separation.

Since the nonlinear three-dimensional solutions are examined near their bifurcation from the basic state, subtracting their axisymmetric component leaves essentially the eigenmode (we refer to this as the perturbation field). In Fig. 12, the perturbation velocity for RW_4 and RW_5 is plotted on horizontal planes at $z=(0.156i-0.031)\Lambda$ for $i\in[1,6]$, showing contours of the perturbation axial velocity, w_p, and projections of the perturbation velocity vectors, (u_p,w_p), onto the planes. The maxima in the perturbation velocities are located about the shear layer, as was indicated by the contours of $\mathcal{E}_m(r,z)$, and it is now clear that these eigenmodes consist of spiral vortical structures of alternating sign. Vertical sections of these spirals are presented in Fig. 13, where the perturbation velocity is plotted in three meridional planes separated by angles $2\pi/3m$, $m=4$, and $m=5$ for RW_4 and RW_5, respectively, covering one azimuthal wavelength for each.

The structures of the complete nonlinear solutions are indicated in Fig. 14. The isosurfaces of the vertical velocity serve to illustrate that, although the three-dimensional perturbation is largest about the separation shear layer near the differentially rotating top, as discussed above. The axisymmetric basic state also has its largest vertical velocity in this region, and so the complete nonlinear state remains nearly axisymmetric here. At lower vertical levels, the balance between the axisymmetric component and the three-dimensional perturbation is such that the three-dimensional structure becomes more evident. By middepth ($z=0.5\Lambda$), the full solution shows the development of funnel-like structures consisting of m vortices rotating with sense opposite to the background rotation (see Ref. [8] for more details).

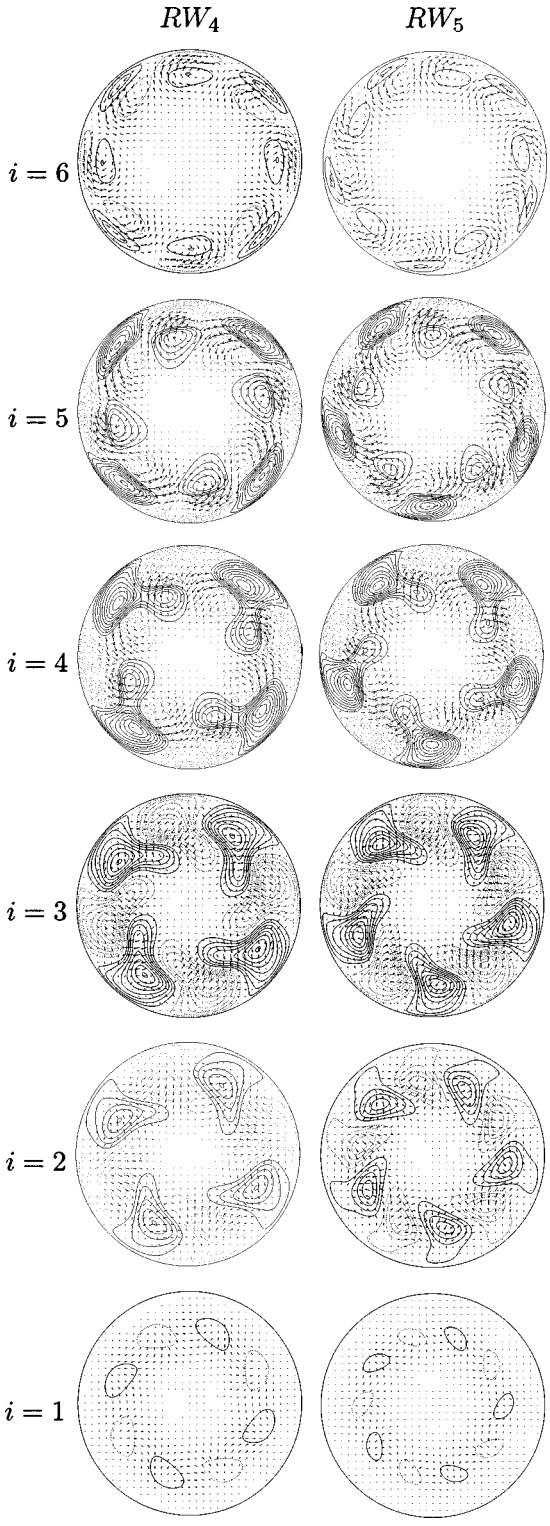

FIG. 12. Contours of the axial velocity perturbation w_p and arrows of the velocity perturbation (u_p, w_p) for (a) RW_4 and (b) RW_5 at ($\mathrm{Re}=365$, $S=1.0$, $\Lambda=0.55$). The six frames show horizontal sections $(r,\theta)\in[0,1]\times[0,2\pi]$, equispaced in the vertical direction with $z=(0.156i-0.031)\Lambda$, $i=1,\ldots,6$.

V. CONCLUSIONS

The competition between rotating wave states with azimuthal wave numbers $m=4$ and $m=5$, bifurcating from an axisymmetric basic state in a rotating cylinder, that is driven by the differential rotation of its upper lid, has been examined. The bifurcation from the basic state is due to the azimuthal instability of the shear layer that is produced by the separation of the boundary layer on the counter-rotating top. The system is governed by three parameters, and the competition between the two modes of instability is organized by a codimension-3 tangent double Hopf bifurcation. Applying the center manifold theorem, we have derived a normal form for this class of codimension-3 bifurcations, and have analyzed the scenario corresponding to the mode competition manifested in our flow problem.

As with the generic double Hopf bifurcation, there are many different scenarios depending on the normal form coefficients which in turn are problem dependent. Competitions between azimuthal modes with wave numbers m and $m+1$ are ubiquitous in flows in cylindrical geometries with internal shear layers. It would be an interesting exercise to explore the dynamics associated with other scenarios of this new tangent double Hopf bifurcation and see if these account for observed dynamics in some of these other systems.

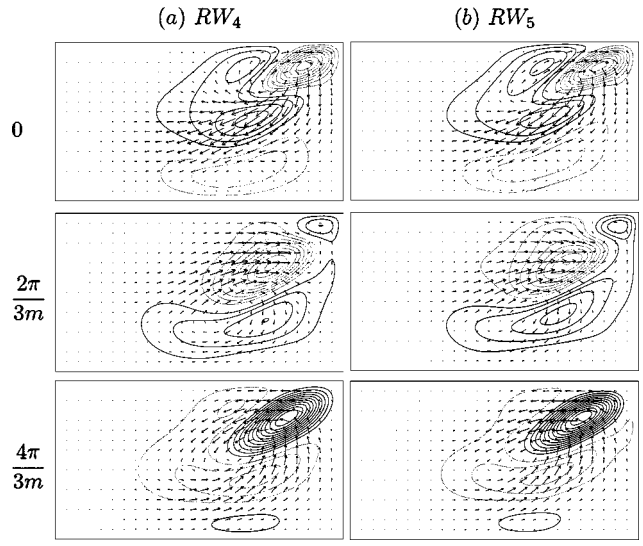

FIG. 13. Contours of the perturbation azimuthal velocity v_p and projections of the perturbation velocity onto three equispaced meridional planes, $(r,z)\in[0,1]\times[0,\Lambda]$, covering one azimuthal wavelength (θ as indicated) for (a) RW_4 and (b) RW_5 at ($\mathrm{Re}=365$, $S=1.0$, $\Lambda=0.55$).

ACKNOWLEDGMENTS

This work was supported by MCYT Grant No. BFM2001-2350 (Spain), the Spanish Foreign Affairs Ministry, the Israel Ministry of Science, the Israel Ministry of Immigrant Absorption, and NSF Grant No. CTS-9908599 (USA).

APPENDIX A: LINEAR STABILITY ANALYSIS OF THE BASIC STATE

The three-dimensional stability problem is solved using the global Galerkin method. Details on this numerical approach can be found in Refs. [22,23]. The solution of Eqs.

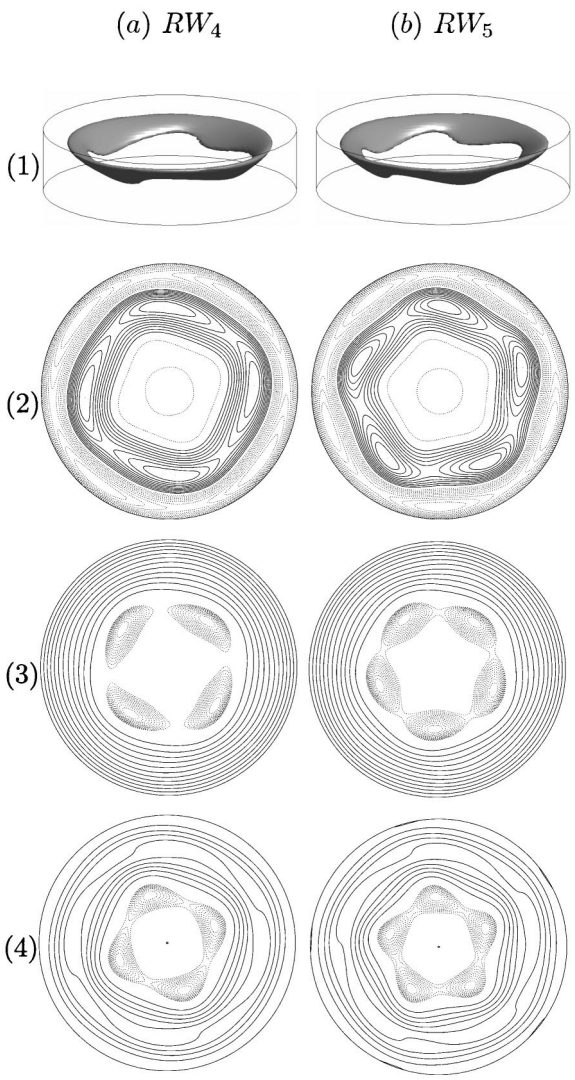

FIG. 14. (1) Isosurfaces of the vertical velocity w at 80% of the maximum downwards value, and contours at $z=0.5\Lambda$ of (2) the axial velocity, (3) the azimuthal velocity, and (4) the axial vorticity, for (a) RW_4 and (b) RW_5 at ($\mathrm{Re}=365$, $S=1.0$, $\Lambda=0.55$). Solid lines correspond to positive values except in (2).

(1), (2), and (4) is expanded in a Fourier series as

$$\{u,v,w,p\}=\sum_{m=-\infty}^{+\infty}\{u_m,v_m,w_m,p_m\}e^{im\theta}, \qquad \text{(A1)}$$

where the Fourier coefficients $\{u_m,v_m,w_m,p_m\}$ are functions of (r,z,t) and their equations are obtained by substitution of Eq. (A1) into Eqs. (1), (2), and (4). The axisymmetric Fourier mode $m=0$ corresponds to both the axisymmetric basic state and the axisymmetric perturbation. The discontinuity where the differentially rotating lid meets the cylinder sidewall at $(r=1,\ z=\Lambda)$ is treated similarly to the case of rotating lid–cylinder flow studied in Refs. [13,23]. The axisymmetric part of the circumferential velocity is represented as

$$v_0(r,z,t)=r\left(1+\Omega_0(r,z)+\sum_{i=1}^{N_r}\sum_{j=1}^{N_z}\alpha_{ij}(t)\phi_{ij}(r,z)\right),$$

where unity corresponds to the background rotation of the whole system and $\Omega_0(r,z)$ is the correction satisfying all the boundary conditions. After the function $\Omega_0(r,z)$ is found, the boundary conditions for the Galerkin basis functions ϕ_{ij} are zero at all no-slip boundaries, and so can be constructed as described in Ref. [22]. The function $\Omega_0(r,z)$ is the solution to

$$\Delta\Omega_0=0,$$

with boundary conditions

$$\Omega_0(r,0)=\Omega_0(1,z)=0, \quad \Omega_0(r,\Lambda)=-1-S.$$

It is approximated as

$$\Omega_0(r,z)=\sum_{i=1}^{M_r}\sum_{j=1}^{M_z}\Omega_{ij}\xi_{ij}(r,z),$$

where the basis functions ξ_{ij} satisfy the zero boundary conditions at $z=0$ and $r=1$. The boundary condition at $z=\Lambda$ is satisfied approximately by introducing M_r Chebyshev collocation points at this boundary. The Laplace equation for $\Omega_0(r,z)$ is introduced to smooth possible wiggles near the discontinuity point. It is solved numerically by projection of its residual on $(M_r-1)M_z$ functions ξ_{ij}. Note that the function $\Omega_0(r,z)$ depends on the governing parameters Λ and S, but does not depend on Re. Thus, for variations in Re only, as is done in the stability analysis, it need only be calculated once for each value of Λ and S.

Resolution tests show that, as in the rotating disk–cylinder flow [13], a sufficiently smooth solution $\Omega_0(r,z)$ can be obtained with $M_r=100$ and $M_z=30$ (the large M_r is needed to resolve the discontinuity in Ω_0 at $r=1$, $z=\Lambda$). With this truncation number the deviation of v_0 from the value $-S$ at 100 uniformly distributed points at the boundary $z=\Lambda$ is less than $10^{-3}S$.

The convergence study for the critical Reynolds number and the critical oscillation frequency shows that at $\Lambda=0.5$ and $S=0.5$, the use of $N_r=N_z=20$ basis functions for all the unknown functions provides three to four converged significant figures for the critical values. Convergence to within five significant figures is obtained with $N_r=N_z=30$. This is illustrated in Table II, which shows the convergence for Fourier azimuthal modes $m=4$ and $m=5$, which are the most critical for $\Lambda=0.5$ and $S=0.5$. Note that the convergence of the critical parameters means convergence of both the steady axisymmetric flow and the three-dimensional perturbation. This rapid convergence is a consequence of the relatively low critical Re, which is usually below 1000 for the range in (Λ,S) considered. In the rotating disk–cylinder flow case, $\mathrm{Re}_c>2000$ requires larger truncation numbers N_r and N_z. The calculations reported here used $N_r=N_z=20$.

TABLE II. Convergence of Re_c and ω_c for $\Lambda=0.5$ and $S=0.5$.

	$m=4$		$m=5$	
$N_r=N_z$	Re_c	ω_c	Re_c	ω_c
10	749.26	−0.26768	761.40	−0.29215
12	743.96	−0.26959	746.95	−0.29708
14	744.35	−0.27062	744.24	−0.29950
16	744.49	−0.27072	743.39	−0.30033
18	744.40	−0.27058	743.04	−0.30045
20	744.35	−0.27047	742.95	−0.30043
22	744.34	−0.27041	742.93	−0.30040
24	744.34	−0.27039	742.93	−0.30038
26	744.34	−0.27038	742.94	−0.30038
40	744.34	−0.27038	742.94	−0.30038

APPENDIX B: THREE-DIMENSIONAL NAVIER-STOKES SOLVER

In order to obtain the bifurcated states and study their dynamics, the full nonlinear time-dependent Navier-Stokes equations (1) and (2) using the nonlinear terms (3) must be solved.

Note that in addition to the nonlinear coupling, the velocity components (u,v) are also coupled by the linear operators. Following Ref. [24], we introduce a new set of complex functions,

$$u_+=u+\mathrm{i}v, \quad u_-=u-\mathrm{i}v,$$

where

$$u=\frac{1}{2}(u_++u_-), \quad v=\frac{1}{2\mathrm{i}}(u_+-u_-).$$

The Navier-Stokes equations (1) and (2) can then be written using (u_+,u_-,w,p) as

$$\partial_t u_+ + a_+ = -\left(\partial_r+\frac{\mathrm{i}}{r}\partial_\theta\right)p+\frac{1}{\mathrm{Re}}\left(\Delta-\frac{1}{r^2}+\frac{2\mathrm{i}}{r^2}\partial_\theta\right)u_+,$$

$$\partial_t u_- + a_- = -\left(\partial_r-\frac{\mathrm{i}}{r}\partial_\theta\right)p+\frac{1}{\mathrm{Re}}\left(\Delta-\frac{1}{r^2}-\frac{2\mathrm{i}}{r^2}\partial_\theta\right)u_-,$$

$$\partial_t w + a_z = -\partial_z p+\frac{1}{\mathrm{Re}}\Delta w,$$

$$\left(\partial_r+\frac{1}{r}\right)(u_++u_-)-\frac{\mathrm{i}}{r}\partial_\theta(u_+-u_-)+2\partial_z w=0,$$

where we have denoted

$$a_\pm = a_r \pm \mathrm{i}a_\theta.$$

We use a stiffly stable semi-implicit, i.e., the linear terms are treated implicitly while the nonlinear terms are explicit, second-order projection scheme [11,25]. For the space variables, we use a Legendre-Fourier approximation. More precisely, the azimuthal direction is discretized using a Fourier expansion with $k+1$ modes corresponding to azimuthal wave numbers $m=0,1,2,\ldots,k/2$, while the axial and vertical directions are discretized with Legendre expansions. With this discretization, a Poisson-like equation for each of the velocity components and the pressure is solved at each time step. The spectral convergence of the code has been extensively tested for this flow in Ref. [8]. All the results presented here have 32 Legendre modes in r and z and 40 Fourier modes in θ, and the time step is $\delta t=0.05$.

APPENDIX C: ANALYSIS OF THE TANGENT DOUBLE HOPF BIFURCATION

In this appendix, we analyze the fixed points of the normal form (11), and their stability. The normal form coordinates ξ_1, ξ_2 are the squares of the radial coordinates r_1, r_2 in Eq. (8), and therefore are always greater than or equal to zero. As the normal form coordinates include two angles, ϕ_1, ϕ_2 with trivial evolution (8), a fixed point at the origin of the (ξ_1,ξ_2) plane is a true fixed point, while fixed points on the axis are periodic solutions and fixed points off the axis are quasiperiodic solutions (two tori). A simple calculation shows that the normal form (11) has four fixed points:

$$P_0:(0,0), \quad P_1:(a\mu_2,0), \quad P_2:(0,\mu_2-\mu_1^2-\mu_3),$$

$$P_3:\left[\frac{\eta-a}{\delta\eta-1}\left(\mu_2-\frac{\eta}{\eta-a}(\mu_1^2+\mu_3)\right)-\frac{\delta a-1}{\delta\eta-1}\left(\mu_2+\frac{1}{\delta a-1}(\mu_1^2+\mu_3)\right)\right].$$

As mentioned before, P_0 is a fixed point, P_1 and P_2 are periodic solutions, and P_3 is a two torus.

$P_0=(0,0)$ exists for all values of the parameters μ_i. In order to analyze their stability, let us consider the Jacobian matrix of the system (11) at P_0,

$$J_{P_0}=\begin{pmatrix} a\mu_2 & 0 \\ 0 & \mu_2-\mu_1^2-\mu_3 \end{pmatrix}.$$

P_0 is stable if and only if $a\mu_2<0$ and $\mu_2<\mu_1^2+\mu_3$. We have two bifurcation curves, $H_1:\mu_2=0$ and $H_2:\mu_2=\mu_1^2+\mu_3$. At these bifurcation curves, P_1 and P_2 are born in Hopf bifurcations; notice that P_1 and P_2 exist only for $a\mu_2\geqslant 0$, $\mu_2\geqslant\mu_1^2+\mu_3$ because of the positivity of the radial coordinates ξ_1, ξ_2. We will assume $a>0$ in order to have P_0 stable for μ_2 sufficiently negative, as we want to recover the behavior of P_0 in the fluid problem we are considering.

Figure 15 shows the two Hopf curves for (a) $\mu_3<0$, (b) $\mu_3=0$, and (c) $\mu_3>0$. P_0 is stable in region (1); in region (2) P_1 exists but not P_2; in region (6) P_2 exists, but not P_1. In the remaining regions, both P_1 and P_2 exist. For $\mu_3<0$, H_1 and H_2 intersect at double Hopf bifurcation points, with coordinates $\mu_1=\pm\sqrt{-\mu_3}$, $\mu_2=0$. The two double Hopf points coalesce for $\mu_3=0$ at the tangent double Hopf point at the origin, and cease to exist for $\mu_3>0$.

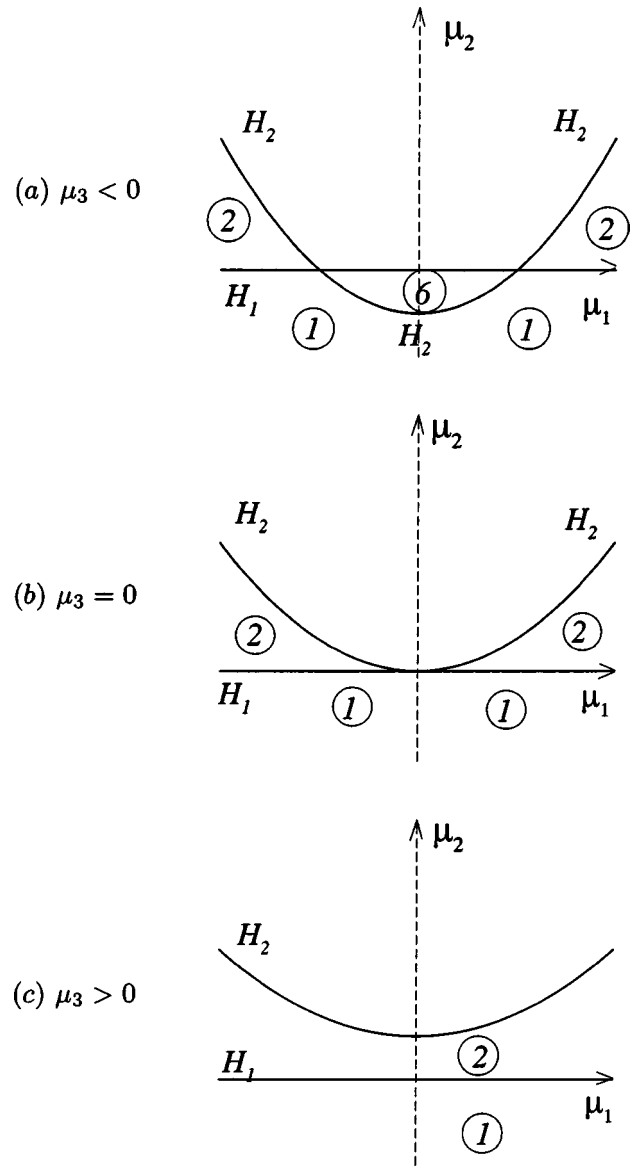

FIG. 15. Hopf bifurcation curves for μ as indicated.

$P_1=(a\mu_2,0)$ exists only above the H_1 curve; its stability is given by the eigenvalues of the Jacobian matrix at P_1,

$$J_{P_1}=\begin{pmatrix} -a\mu_2 & a\eta\mu_2 \\ 0 & \mu_2-\mu_1^2-\mu_3-\delta a\mu_2 \end{pmatrix}.$$

The eigenvalues are $\lambda_1=-a\mu_2<0$ and $\lambda_1=\mu_2-\mu_1^2-\mu_3-\delta a\mu_2$; P_1 is stable if and only if $(1-\delta a)\mu_2<\mu_1^2+\mu_3$. Therefore we obtain another bifurcation curve, $N_1:\mu_2=-(\mu_1^2+\mu_3)/(\delta a-1)$; it is a Neimark-Sacker bifurcation where the periodic solution P_1 bifurcates to a two-torus P_3. For consistency with the numerical results of the fluid problem considered, we will assume $\delta a>1$. The parabola N_1 is directed downwards, and intersects H_1 and H_2 at the two double Hopf bifurcation points, as can be seen in Fig. 4(a). For $\mu_3\geqslant 0$, N_1 does not play any role, because it is entirely contained in region (1), where P_1 does not exist. P_1 is stable above the N_1 bifurcation curve, and unstable below.

$P_2=(0,\mu_2-\mu_1^2-\mu_3)$ exists only above the H_2 curve; its stability is given by the eigenvalues of the Jacobian matrix at P_2,

$$J_{P_2}=\begin{pmatrix} (a-\eta)\mu_2+\eta(\mu_1^2+\mu_3) & 0 \\ \delta(\mu_1^2+\mu_3-\mu_2) & \mu_1^2+\mu_3-\mu_2 \end{pmatrix}.$$

The eigenvalues are $\lambda_1=(a-\eta)\mu_2+\eta(\mu_1^2+\mu_3)$ and $\lambda_2=\mu_1^2+\mu_3-\mu_2<0$; P_2 is stable if and only if $(a-\eta)\mu_2+\eta(\mu_1^2+\mu_3)<0$. Therefore we obtain another bifurcation curve, $N_2:\mu_2=(\mu_1^2+\mu_3)\eta/(\eta-a)$; it is a Neimark-Sacker bifurcation, where the periodic solution P_2 bifurcates to a two-torus P_3. For consistency with the problem considered, we will assume $\eta>a$; and as we have already assumed $a>0$, we also have $\eta>0$. The parabola N_2 is directed upwards, and intersects H_1 and H_2 at the two double Hopf bifurcation points for $\mu_3<0$, as can be seen in Fig. 4(a). For $\mu_3=0$ the three curves H_1, H_2, and N_2 become tangent at the origin [see Fig. 4(b)] and for $\mu_3>0$ they do not intersect any longer [see Fig. 4(c)]. P_2 is stable above the N_2 bifurcation curve, and unstable below.

In order to analyze the stability of the two-torus solution P_3, we introduce two auxiliary combinations of the parameters μ_i,

$$g_1=\mu_2-\frac{1}{\delta a-1}(\mu_1^2+\mu_3),\quad g_2=\mu_2-\frac{\eta}{\eta-a}(\mu_1^2+\mu_3).$$

The N_1 and N_2 bifurcation curves obtained previously are given by $g_1=0$ and $g_2=0$, respectively. Writing P_3 and the Jacobian matrix at P_3 in terms of g_1, g_2 we obtain

$$P_3:\frac{1}{\delta\eta-1}[(\eta-a)g_2,\ (\delta a-1)g_1],$$

$$J_{P_3}=\frac{1}{\delta\eta-1}\begin{pmatrix} -(\eta-a)g_2 & -\eta(\eta-a)g_2 \\ -\delta(\delta a-1)g_1 & -(\delta a-1)g_1 \end{pmatrix}.$$

The eigenvalues λ_1, λ_2 are the solutions of the quadratic equation

$$\lambda^2+\left(\frac{\eta-a}{\delta\eta-1}g_2+\frac{\delta a-1}{\delta\eta-1}g_1\right)\lambda-\frac{(\eta-a)(\delta a-1)}{\delta\eta-1}g_1g_2=0,$$

and satisfy

$$\lambda_1+\lambda_2=-\frac{\eta-a}{\delta\eta-1}g_2-\frac{\delta a-1}{\delta\eta-1}g_1<0,$$

$$\lambda_1\lambda_2=-\frac{(\eta-a)(\delta a-1)}{\delta\eta-1}g_1g_2.$$

Therefore, $\mathrm{sgn}(\lambda_1\lambda_2)=-\mathrm{sgn}(\delta\eta-1)$. If $\delta\eta-1>0$, one of the λ_i is positive, and P_3 is unstable; if $\delta\eta-1<0$, both λ_i are negative, and P_3 is stable. As in the problem considered

here, the two-torus P_3 is never observed close to the tangent double Hopf bifurcation, and so we conclude that $\delta\eta-1>0$. P_3 only exists above both curves N_1, and N_2, and it is unstable. The complete bifurcation diagram including H_1, H_2, N_1, and N_2 is shown in Fig. 4. Phase portraits including the interconnections and stability of the solutions P_i in the six different regions that appear in Fig. 4 are shown in Fig. 3.

During the preceding discussion, we have obtained several inequalities between the constants a, η, δ appearing in the normal form (11). They are $a>0$, $\delta a>1$, $\eta>a$, and $\delta\eta-1>0$. They can be summarized as

$$\eta>a>\frac{1}{\delta}>0, \tag{C1}$$

and, in particular, the three constants are positive.

[1] R. Hide and C.W. Titman, J. Fluid Mech. **29**, 39 (1967).
[2] J.M. Chomaz, M. Rabaud, C. Basdevant, and Y. Couder, J. Fluid Mech. **187**, 115 (1988).
[3] G. Gauthier, P. Gondret, F. Moisy, and M. Rabaud, J. Fluid Mech. **473**, 1 (2002).
[4] W.-G. Früh and P.L. Read, J. Fluid Mech. **383**, 143 (1999).
[5] I.M. Moroz and P. Holmes, J. Atmos. Sci. **41**, 3147 (1984).
[6] S.M. Churilov and I.G. Shukhman, J. Fluid Mech. **243**, 155 (1992).
[7] P. Chossat and G. Iooss, *The Couette-Taylor Problem* (Springer, New York, 1994).
[8] J.M. Lopez, J.E. Hart, F. Marques, S. Kittelman, and J. Shen, J. Fluid Mech. **462**, 383 (2002).
[9] J.M. Lopez, J. Fluid Mech. **359**, 49 (1998).
[10] J. Sanchez, F. Marques, and J.M. Lopez, J. Comput. Phys. **180**, 78 (2002).
[11] J.M. Lopez, F. Marques, and J. Shen, J. Comput. Phys. **176**, 384 (2002).
[12] J.M. Lopez, J. Fluid Mech. **221**, 533 (1990).
[13] A.Y. Gelfgat, P.Z. Bar-Yoseph, and A. Solan, J. Fluid Mech. **311**, 1 (1996).
[14] J.E. Marsden and M. McCracken, *The Hopf Bifurcation and Its Applications* (Springer, New York, 1976), Vol. 19.
[15] G. Iooss and M. Adelmeyer, *Topics in Bifurcation Theory and Applications*, 2nd ed. (World Scientific, Singapore, 1998).
[16] S. Wiggins, *Introduction to Applied Nonlinear Dynamical Systems and Chaos* (Springer, New York, 1990).
[17] Y.A. Kuznetsov, *Elements of Applied Bifurcation Theory*, 2nd ed. (Springer, New York, 1998).
[18] F. Marques, J.M. Lopez, and J. Shen, J. Fluid Mech. **455**, 263 (2002).
[19] T. Mullin and C. Blohm, Phys. Fluids **13**, 136 (2001).
[20] J.M. Lopez, F. Marques, and J. Shen (unpublished).
[21] J. Guckenheimer and P. Holmes, *Nonlinear Oscillations, Dynamical Systems, and Bifurcations of Vector Fields* (Springer, New York, 1997).
[22] A.Y. Gelfgat, Comput. Fluid Dyn. J. **9**, 437 (2001).
[23] A.Y. Gelfgat, P.Z. Bar-Yoseph, and A. Solan, J. Fluid Mech. **438**, 363 (2001).
[24] S.A. Orszag and A.T. Patera, J. Fluid Mech. **128**, 347 (1983).
[25] J.M. Lopez and J. Shen, J. Comput. Phys. **139**, 308 (1998).